PHYSICAL REVIEW APPLIED **6,** 044003 (2016)

Intrinsic Trade-off between Up-Conversion and Trapping Rates in InAs Quantum Dots for Intermediate-Band Solar Cells

David M. Tex,[1] Kouichi Akahane,[2] and Yoshihiko Kanemitsu[1,*]

[1]*Institute for Chemical Research, Kyoto University, Uji, Kyoto 611-0011, Japan*
[2]*National Institute of Information and Communications Technology, Koganei, Tokyo 184-8795, Japan*

(Received 13 July 2016; revised manuscript received 12 August 2016; published 3 October 2016)

High-density InAs quantum-dot (QD) layers are extensively used for testing intermediate-band solar cells based on two-step two-photon-absorption (TS-TPA) up-conversion processes. Here, photocurrent (PC), photoluminescence, and atomic-force microscopy are used to clarify the limitation of the high-density InAs QD approach. We measure two-color-beam PC spectra on InAs QD layers with QD densities ranging from 0.5 to $4.6 \times 10^{10}/\mathrm{cm}^2$. It is shown that the high-density QD layer has a reduced PC-generation efficiency, and that the TS-TPA PC is reduced by trapping, rather than recombination.

DOI: 10.1103/PhysRevApplied.6.044003

I. INTRODUCTION

As has been rigorously shown, the single-junction solar cells obey the Shockley-Queisser limit [1]. To exceed classical limits, alternative device-design principles are essential [2]. By understanding the physical limitations of the current generation processes, more-complex devices are able to outperform the simple structures, as has been demonstrated with the tandem approach [3], and is also prospected for radial junctions [4–6]. Still, even in conventional structures, the current-generation processes have to be investigated further to reach the limits [7–11].

The intermediate-band (IB) solar cells have been proposed as another fascinating alternative approach for reaching high conversion efficiencies. They employ conversion of subband-gap photons [mainly infrared (IR)] into current by up-conversion [12]. The commonly considered up-conversion process is the two-step two-photon-absorption (TS-TPA) process, where two photons are sequentially absorbed to promote an electron from the valance band to an IB, and then to the conduction band of the bulk matrix [13].

Many structures have been proposed for realizing the IB solar cell [14]. One of the most anticipated approaches is the use of quantum dots (QDs) [15], which provide wide-range subband photocurrent (PC) generation [16]. Unfortunately, the experimentally obtained efficiencies are far from the predicted 63% [13,17–24]. The problem is that the observed PC induced by TS-TPA transitions is too small to maintain a nonequilibrium condition; i.e., thermal-excitation and -trapping rates are much higher than the TS-TPA rate [22,24–29]. Therefore, improvement of the IR absorption coefficient is required to produce high-efficiency devices.

To solve this problem, band formation, doping, crystal quality, and dot densities have been investigated theoretically and experimentally [18–21,23,30–33]. It is usually considered that an increase in absorption up to $10^4/\mathrm{cm}$ in both visible and IR regions is possible only by introducing high QD densities on the order of $10^{11}/\mathrm{cm}^2$.

Still, even in high-quality samples, the trapping rates are confirmed as being too fast for a significant TS-TPA PC [28], suggesting an intrinsic problem. Independent of the sample structure, it has been shown that a reduction in the PC upon additional IR illumination can occur under certain excitation conditions [27,34], indicating that the TS-TPA up-conversion efficiency is limited by the intrinsic carrier-extraction efficiency, rather than absorption. The question is, whether high QD densities can compensate for the low extraction efficiency and whether this problem is simply one of either enhanced nonradiative recombination or another physical effect. To clarify the feasibility of the high-density InAs QD approach, the PC-generation mechanism has to be investigated with a two-color-beam experiment combining variable QD densities and excitation-light sources.

In this work we reveal the influence of the QD density on the TS-TPA up-conversion efficiency. Using photoluminescence (PL) and atomic-force microscopy (AFM), the QD densities in three different samples are quantified and an almost-constant nonradiative recombination rate for all samples is confirmed. To understand the IB operating principle, we measure two-color-beam PC spectra. By increasing the QD density from $5 \times 10^9/\mathrm{cm}^2$ to $4.6 \times 10^{10}/\mathrm{cm}^2$—i.e., by a factor of 10—the single-dot PC contribution decreased superlinearly by a factor of 30. This result proves that there exists a trade-off between absorption and current-extraction efficiency, depending on the QD density. The low TS-TPA efficiency in dense QDs is a result of trap charging, rather than enhanced nonradiative recombination. It is shown that the low-density QD layer performs far better than the high-density layers. Therefore, we consider that the intrinsic properties of the single QDs are excellent. However, the implementation of

---

[*] kanemitu@scl.kyoto-u.ac.jp

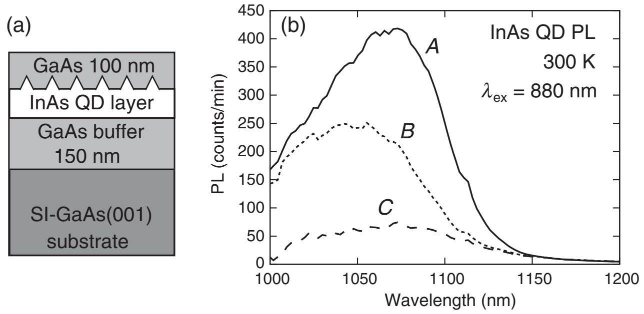

FIG. 1. (a) Sample structure. The QD densities are changed from high (sample A) to intermediate (sample B) and low (sample C). (b) Room-temperature InAs QD PL.

the QD for realizing high-efficiency IB solar cells has to be reconsidered. Instead of increasing QD densities, their location has to be controlled precisely.

II. EXPERIMENTAL

The samples investigated in this work are grown by molecular-beam epitaxy (Veeco GEN II). The sample structure is shown in Fig. 1(a). A GaAs buffer with 150 nm thickness is grown on top of a semi-insulating (SI) GaAs(001) substrate. Then the InAs QD layer is grown and capped with a GaAs layer. Three different InAs layers are prepared: sample A has a high QD density [an InAs deposition amount equivalent to 2 monolayers (MLs) at 450 °C], sample B an intermediate QD density (2 ML InAs at 500 °C), and sample C a low QD density (1.4 ML InAs at 500 °C).

To analyze the suitability of the different QD layers for solar-cell application, single- and two-beam PC spectra are measured. The single-beam-PC baseline data is taken with a tunable monochromatic-light source with a power of about 200 μW and a spot size of about 200 μm. To probe the carrier-generation efficiency via TS-TPA processes from the quantum structure to the bands, we use a second IR beam at 1550 nm with 400 μW as an additional excitation source and measure the change in PC. For the electrical measurements, the samples are cut into pieces of about 10×10 mm and attached on a Cu plate using a conducting Ag paste. A rectangular 2×2-mm- and about 300-nm-thick Au electrode is sputtered on top of the samples. The PC measurements are performed using various bias voltages up to 1 V, which corresponds to an electric field of 30 V/cm throughout the sample in the dark condition. The contact characteristics are investigated with I-V curves, and it is confirmed that there is no influence on our results (details are shown in Appendix C).

III. QD DENSITIES

The PL spectra for excitation with 880 nm at 300 K are shown in Fig. 1(b). To remove the impurity PL background, the PL taken from a GaAs substrate is subtracted. We observe strong QD PL from sample A, intermediate QD PL from sample B, and weak QD PL from sample C. From the PL area, we estimate the ratio of the QD densities in the three samples as about $A:B:C = 3.3:2:0.6$. The validity of this estimation is confirmed by AFM measurements on uncapped samples grown under the same conditions (explained below).

The AFM images are shown in Figs. 2(a) to 2(c). The upper half of the images is used to outline the monolayer-step features of the wetting layer (WL) and the thicker 2- and 3-ML structures [35]. Figure 2(a) shows the high-density QD layer, (b) the intermediate-density QD layer, and (c) shows the low-density QD layer. The details of the AFM analysis are given in Appendix A. The QD densities and different monolayer areas are summarized in Table I. Sample A has about a 10-times-higher QD density than sample B. Sample C has no QDs. We note that the overall QD densities may be reduced due to surface migration and the desorption of In and As from the surface during the cooling process. To analyze the amount of evaporated InAs of the uncapped samples, we calculate the equivalent deposited amount of InAs from the QD volume, the 1-ML WL, and the 2- and 3-ML island volumes. The total volume of sample A is 1.98 ML, which is very close to the

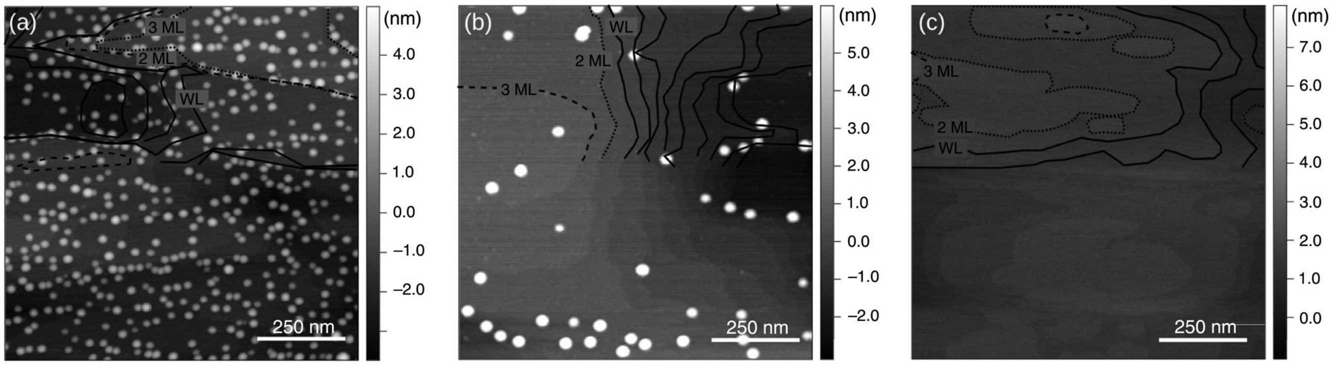

FIG. 2. AFM images of (a) high-, (b) intermediate-, and (c) low-QD-density layers. The top half of the figures outlines the monolayer steps and identifies the wetting and multiple monolayers.

TABLE I. Summary of QD, WL, and 2- and 3-ML island properties determined by AFM.

	Sample *A*	Sample *B*	Sample *C*
QD density	Approximately 456 μm^{-2}	46 μm^{-2}	0
QD height	4.6 nm	10.3 nm	⋯
1-ML WL area	83%	72%	72%
2-ML area	7%	18%	26%
3-ML area	10%	10%	1%
QD volume	0.71 ML	0.27 ML	0 ML
WL volume	1.27 ML	1.38 ML	1.27 ML
Total volume	1.98 ML	1.65 ML	1.27 ML
Deposited InAs	2 ML	2 ML	1.4 ML
Volume difference	0.02 ML	0.35 ML (143 QDs)	0.13 ML (53 QDs)

nominal deposited 2 ML. No significant evaporation occurred for this sample. The total volume of sample *B* is 1.64 ML, which is significantly different from the nominal deposited 2 ML. This volume would correspond to 60 large QDs (as observed in sample *B*) or 225 small QDs (as observed in sample *A*). We consider that the average is suitable for discussion and, therefore, in sample *B*, about 143 QDs are lost during the cooling process. Also, for sample *C*, a significant difference is observed. The loss would correspond to about 53 QDs.

From AFM, we find a ratio of QD densities for the three samples of 4.6∶1.9∶0.5, which is in fair agreement with the PL results. In the high-density sample, PL seems to be slightly quenched due to carrier transfer, but overall it is confirmed that the nonradiative rates are almost the same for all of the samples.

The AFM images show that the morphology of the InAs layer is complex. As a result, the PL and PC spectra of InAs layers are rather difficult to interpret due to the coexistence of WL and QD structures. Therefore, we investigated the energy levels and the PC-generation processes in InAs layers using spectroscopic methods [27,36–42]. The results enable a clear assignment of the different energy levels to those of the WL and QD structures, which are discussed in the next section.

IV. PHOTOCURRENT SPECTRA

Now we compare the room-temperature PC spectra for a 1-V bias, which are shown in Figs. 3(a)–3(c). The PC values are converted to external quantum efficiency (EQE) by normalizing with the input photon flux of the primary beam. The baseline for the high-density QD sample *A* with single-beam excitation is shown in Fig. 3(a) by the dotted line. For excitation below 880 nm (GaAs band gap), we observe a constant response from GaAs. The GaAs PC is small since we use a SI substrate, intentionally doped to increase the resistivity of the sample. From 880 to 920 nm, we observe a strong increase in the PC due to the excitation of 2-ML-thick WL structures, which have a strong PC response [37]. The dip structure slightly above 880 nm is a result of the weak absorption between the GaAs band edge and the lower-lying states. From 920 to 1100 nm, a gradual decrease in the PC is observed. This region corresponds to the QD region, and the decrease of the PC for longer wavelengths is a result of the QD energy distribution. For longer wavelengths, the PC levels off and is almost zero.

The PC for the two-beam excitation of sample *A* is shown by the solid line in Fig. 3(a). The additional IR beam has low photon energy, which cannot excite the GaAs and InAs quantum structures directly but contributes to the PC via TS-TPA processes. Therefore, we see a PC enhancement in the GaAs region due to a reactivation of trapped carriers via TS TPA. For the 2-ML-thick WL excitation, no change is observed, which is explained by strong thermal activation from these shallow states. In the QD region, a significant change of the PC level due to the activation of carriers via TS TPA is again observed. Under the present conditions, we observed a reduction in the total PC. For longer excitation wavelengths, the IR beam leads again to a PC increase. The deep-trap levels in GaAs can contribute to

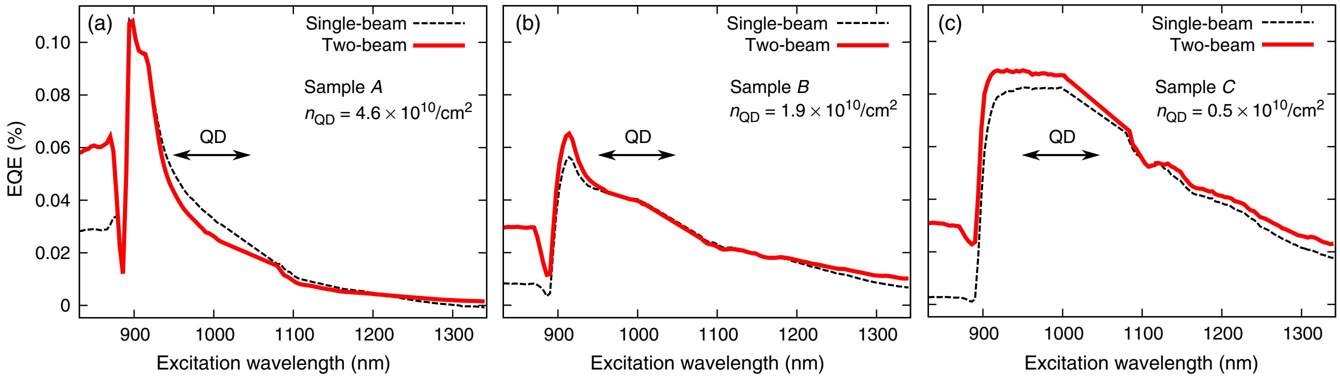

FIG. 3. Single- and two-beam PC spectra at room temperature for (a) sample *A*, (b) sample *B*, and (c) sample *C*. The dotted line is the baseline for single-beam excitation with the tunable monochromatic-light source (200 μW). The solid line is the value measured under simultaneous excitation with the monochromatic light (200 μW) and the IR beam at 1550 nm (400 μW).

PC due to additional carrier activation under IR illumination [43]. The varying spectral response of the IR beam proves that the peculiar EQE response in the QD region is not simply the result of the excitation of deep traps in GaAs.

The single-beam response of sample *B* is shown in Fig. 3(b). When compared to the results from sample *A*, both the GaAs and WL PC levels decreased by about a factor of 2. The decrease of the GaAs and WL baseline current is considered to be a result of a smaller number of shallow Shockley-Read-Hall recombination centers provided by the WL for higher QD densities. For IB solar cells it is important that the contribution of the QDs to the PC increased relatively to sample *A*. In the two-beam experiment, shown by the solid line, we confirm that the PC exhibits almost no change in the QD region for additional IR excitation.

For the low-density sample *C*, shown in Fig. 3(c), the QD PC contribution under single-beam excitation (the dotted line; about 1000 nm) is now very large compared to the high-density QD layer. Additionally, the two-beam excitation data (the solid line) shows a significant enhancement of the PC.

The dense QD layer is usually intended to improve the absorption and enhance the TS-TPA PC response. However, the PC generation from the dense QD layer (sample *A*) via the primary beam is 2.54 times weaker than that of the almost-10-times-sparser layer (sample *C*). The PC reduction for high densities is even larger when adding the IR beam (3.33 times weaker). The absolute values of the PC vary depending on the excitation-geometry and sample conditions. To understand the influence of the QD density on the conversion efficiencies, it is most appropriate to discuss the results in comparison to the low-density sample *C*. We find that the relative tendency of lower EQE for higher QD densities is the same even for different experimental conditions, as shown in Figs. 6(a) and 6(b) in Appendix B. The reduction of the IR response has important implications for the design of QD IB solar cells. To clarify how to proceed with the QD IB solar cell, the physical origin of the PC reduction must be understood first.

V. QD TRAPPING

We consider that the lower PC EQE for higher QD densities is a result of hole capture by traps of QDs and not by a difference in nonradiative rates, as confirmed by PL and AFM. The even more drastic PC reduction for additional IR excitation is the result of eventual charging of the QDs by removal of the electron by the IR beam. This model is also supported by the experimental power dependence, as shown in Figs. 4(a) and 4(b). The absolute values in Figs. 3(a)–3(c) and Figs. 4(a) and 4(b) cannot be compared directly since the PC intensity depends on excitation-geometry and sample conditions. However, the density dependence of the relative changes is quite similar, as confirmed below.

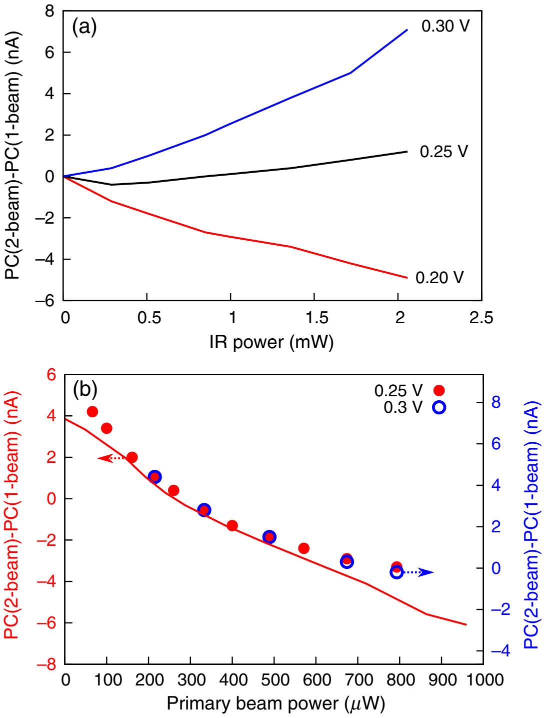

FIG. 4. (a) Power dependence of absolute PC change due to the secondary IR beam for different voltages. The primary beam is set to 1020 nm, exciting the QDs with 260 μW. (b) Power dependence of absolute PC change due to the primary beam for different voltages. The secondary beam is set to 1.5 mW. The line is the theoretical curve, as explained in the text, but it is rescaled for easy comparison of the relative trends.

The power dependence of the two-beam PC response of the QDs with respect to the IR beam is shown in Fig. 4(a). Compared to the EQE at high voltages (0.3 V, the blue data), the conversion efficiency is lowered for a lower bias voltage (0.25 and 0.2 V), which means that the electrical field plays a major role in the observed phenomena. The saturation behavior of the IR PC response for all voltages suggests that the reduction is a result of the charging of a limited number of traps.

The power dependence of the two-beam PC response with respect to the primary beam is shown in Fig. 4(b). Compared to the PC EQE under low-QD ground-state excitation, a significant reduction in the PC EQE is observed for higher excitation powers. The same reduction for a higher QD population is observed at low and high voltages (0.25 and 0.3 V), and a saturation occurs at high powers.

The decrease of the conversion efficiency for higher QD ground-state excitation can be explained by a charging of the traps. We consider that the IR beam can only excite electrons from the QD state to the conduction band. The probability of finding an electron in the QD is proportional to the ground-state excitation. Therefore, the charging rate is directly proportional to the primary beam. Consequently, efficiency improvement by IR illumination is reduced for stronger QD excitation.

The charging of the traps results in a reduction of the separation efficiency in bias direction due to Coulomb force, which can become significantly large for high QD densities. If the separation efficiency becomes very small, a PC reduction upon additional IR illumination can be observed, as has been already reported previously and is also seen in Fig. 3(a), where the two-beam PC from the QDs is lower than that for single-beam excitation [27,34]. The power dependence shows that the absolute value of the IR PC response can be controlled by the electrical field. However, the charging of the trap states always leads to a reduction in the IR photon-conversion efficiency, as is evident from the curvature of the power dependence.

To support the trap-charging model with quantitative numbers, we perform a self-consistent calculation in the next section. The result of the self-consistent calculation is shown by the curve in Fig. 4(b). To allow for an easy comparison of the trends, the curve is rescaled. The agreement of the efficiency reduction for a higher QD population means that the results from the power dependence are consistent with the results shown in Figs. 3(a)–3(c).

Instead of varying the QD ground-state excitation, we can also change the density of the QDs by exchanging the samples, which should lead to a similar trend. The experiment is performed with the 1550-nm IR beam, exciting only deep traps in GaAs. According to our model, a part of these carriers should be trapped in the deep traps of the InAs layer, leading to band bending and reduction of the PC.

The total PC is measured at the 1-V bias for samples *A*, *B*, and *C*, and a reference GaAs substrate. The dark current is about 30 nA for all samples. The experimental conditions are the same as for Fig. 3. The PC for the reference GaAs is $I_{\mathrm{GaAs}} = 46.9$ nA. In comparison, the PC is reduced for the samples with InAs layers, which is due to the higher number of traps (proportional to the QD density). The data points for the PC are given by the dots in Fig. 5. Sample *C* had about half of the GaAs PC and sample *B* one sixth, while sample *A* showed a reduction of the current due to IR illumination by about one tenth of the GaAs PC. The data points for an experiment performed on an aged sample are given by the open squares. We observe the same inclination with a reduced PC for higher QD densities, showing that this inclination is intrinsic to the QDs. Based on the power dependence, we propose that the reduction of the PC upon IR illumination is due to a change in the band profiles as a result of the charging of the traps.

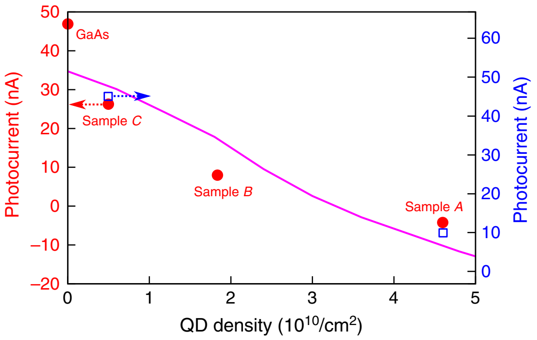

FIG. 5. Total PC induced by the IR light only for different QD densities. Closed circles and open squares are the results of different experiments, as explained in the text. The line is the theoretical prediction of the QD density dependence of the PC, based on a model of the charging of QD traps. The *x* scale is based on the AFM measurements.

VI. THEORETICAL MODEL

The above data are compared with self-consistent results from the one-dimensional continuity equation. The model considers a 30-μm-thick GaAs layer with a QD-trap layer buried 500 nm below the front side, a bias voltage of 0.1 V, and Ohmic contacts. Details are given in Appendix D. The calculated curve shown by the line in Fig. 5 is in good agreement with the experimental data. By increasing the QD-trap density, the current is reduced and eventually drops below the dark-current level. The charged QD interface forces a redistribution of electrons centered around the QD layer, whose density profile induces a negative diffusion current, which can overcome the drift velocity in the high-field regime. We understand now that the EQE reduction is intrinsic to the charging of QD traps, but the critical density for the PC sign change depends on the QD location in the sample.

The experimental QD-density dependence of the PC spectra evidences that the traps which reduce the IR-beam response are due to the InAs QDs. However, the trap itself may be localized in the GaAs matrix surrounding the QD, which is supported by recent data on a QD solar-cell device [34]. Previously, the reduction of the PC upon IR illumination was assigned to an unknown state in GaAs [34], and our work clarifies that this state is actually induced by the QD growth. The QD growth process is still an issue for the IB solar cell. The relative reduction in the PC upon IR illumination and QD densities in the previous work are comparable to our data. Therefore, we believe that our results represent a general issue in state-of-the-art InAs layers. We consider that the relatively weak field in our samples simulates the working condition of a device under concentrated illumination.

Since the traps are inherently connected with the QD growth procedure, even highly optimized designs suffer from significant TS-TPA losses [18,34]. Device structures often use doping to control the absorption and trapping properties. Although doping is a way to improve the IR absorption [31,33,44,45], doping is not essential for the IB operation principle itself [46]. The moderate doping of the IB states showed improved short-circuit current and open-circuit voltage of the devices—mainly due to a reduction of nonradiative recombination [21,23,47]—rather than an improvement of the up-conversion efficiency. These results suggest that the effect of doping is strongly sample dependent. However, with respect to the IR up-conversion efficiency, we consider that fixed ionized donors behave similar to charged QDs. Another important point for devices is stacking. While the QD absorption increases with a stacking of high-density QD layers, the randomly located QDs should also lead to a strong retrapping of electrons from other layers.

Considering these facts, the conventional implementation of high-density QDs in IB solar cells is difficult. A smart implementation of the QDs in the IB solar cell is required. As shown in Fig. 3(c), the low-density QD layer largely outperforms the high-density layers. Even though the number of QDs in sample *C* is 10 times smaller than in *A*, the PC is 3 times higher. Since the QD spacing in sample *C* is on the order of a few hundred nanometers, the single character of the individual QDs is still preserved. The close spacing in the high-density layers introduces a superlinear trapping effect and leads to a reduction in PC upon additional up-conversion by IR. The high TS-TPA efficiency of the single QD has to be made accessible to the IB solar cell via new device designs, suppressing any charging of traps through a smart alignment of the QDs and reducing the Coulomb force by dilute stacking.

Our results should be relevant for up-conversion systems consisting of two or more intermediate levels, where the IR beam selectively excites one carrier type via TS TPA. During the up-conversion process in such systems (which means the ejection of the electron), the hole stays in the intermediate state, and thus this state is charged upon IR illumination. For optimal IR up-conversion efficiencies, we require a design where no localized charges are created due to IR illumination.

VII. CONCLUSION

In summary, we epitaxially grow InAs/GaAs layers with different QD densities. Two-color-beam PC measurements are used to analyze the QD-density dependence of the TS-TPA mechanism. We find that higher QD densities lead to strongly reduced TS-TPA PC, in contrast to the requirement for the IB solar cell. The PC for QD ground-state excitation in the dense layer is reduced by 21 times, and the additional IR illumination leads to a PC reduced by 28 times when compared to the single QD performance of the low-density layer.

Our data prove that the TS-TPA PC reduction is due to the InAs QD growth. We explain the weak PC extraction efficiency in dense QDs quantitatively with the trapping and charging of traps in GaAs, induced by the QD growth. On the other hand, we find excellent TS-TPA properties for the low-density QD layer. To realize highly efficient QD IB solar cells, the trade-off between high-density and current-extraction efficiency, reduced by Coulomb force, has to be considered. The low-density QD-layer design shown here seems to be most suitable.

ACKNOWLEDGMENTS

Part of this work was supported by JST-CREST.

APPENDIX A: ATOMIC-FORCE MICROSCOPY

The uncapped samples [Figs. 1(a)–1(c)] are prepared for an investigation of the InAs layer with atomic-force microscopy (AFM, Bruker AXS Dimension Icon) under normal atmospheric conditions. Since AFM images contain scanning artifacts due to scanner geometry, thermal drift, and vibrations, an appropriate image flattening has to be performed [48]. In the case of images containing nanostructures, these regions have to be excluded to effectively flatten the underlying substrate [49]. The flattening procedure has been carefully performed by excluding the QD areas, in order to reveal the subtle ML step features of the WL and the thicker 2- and 3-ML structures [35]. Because of the strain-driven growth mechanism, many QDs are located at the edges of the layers. The topmost island structure is assigned to the 3-ML-thick InAs layer, which is situated on slightly larger 2-ML regions. Both of these island structures grow on top of the 1-ML-thick WL.

APPENDIX B: GENERAL TREND OF IR BEAM RESPONSE

Figure 6(a) shows the EQE enhancement due to the IR beam for two different excitation conditions. The squares

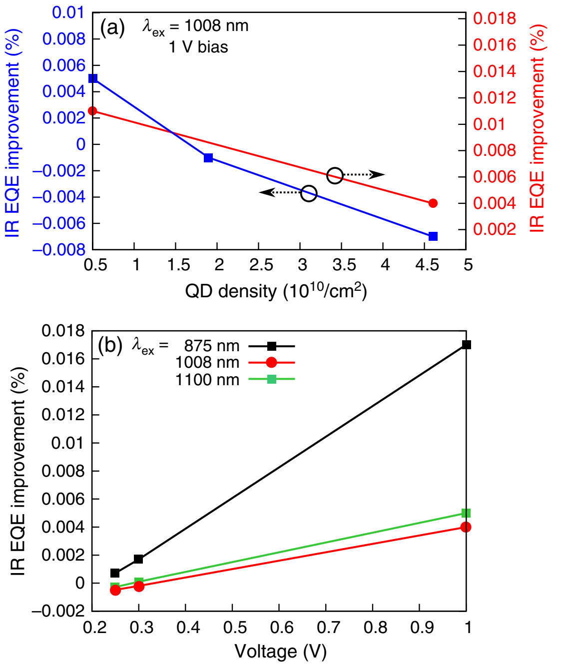

FIG. 6. (a) EQE improvement induced by the IR beam via TS-TPA processes for different excitation conditions of the QD. The circles and squares are results for different experiments, as explained in the text. (b) EQE improvement for different voltages and excitation wavelengths using sample *C*.

represent data for the QD excitation extracted from Figs. 3(a)–3(c). The circles are from another experiment on aged samples. Both experiments use similar excitation fluences and result in the same rate of decrease for higher QD densities, which means that this result is intrinsic to the QDs and is not a side effect of the experimental conditions. Figure 6(b) shows the voltage dependence of the TS-TPA response for the aged sample *C* using different excitation wavelengths. We find that the QD excitation (red data) results in a small TS-TPA response for all voltages, and the TS-TPA response can even reverse its sign for low voltages, similar to the case in Fig. 3(a).

APPENDIX C: CURRENT-VOLTAGE (*I-V*) CURVES

The influence of the electrical contact on the observed trends is investigated with *I-V* curves. A positive voltage means that the hole flows to the top surface and the electrons to the back side of the sample. The dark *I-V* curves in Fig. 7(a) show weak Schottky behavior. We find that the inclination of the data for positive voltages corresponds to the electron mobility. While sample *C* crosses 0 nA at 0 V, sample *A* requires a positive voltage of about 0.1 V to stop the current flow. We consider that the back side of the substrate is almost Ohmic. In this case, the dark *I-V* curve of sample *A* can be explained with a downward bending of the band at the surface due to a trapping of the charges in the high-density QDs in this sample.

The *I-V* curves for the excitation of GaAs are shown in Figs. 7(b) and 7(c) for samples *C* and *A*, respectively. In order to compare the IR responses with the main text, the current values are converted into an EQE value by subtracting the dark current and are normalized by the input photon flux of the primary beam. In both cases, Schottky behavior is observed. Upon excitation with IR, only the 0 nA crossing of sample *A* shifts to higher voltages. This behavior is considered to be the result of larger band bending upon IR excitation in sample *A*, which is possible due to the enhanced ionization of the QDs by the IR beam.

The *I-V* curves for excitation of the 2-ML WL structures in sample *A* are shown in Fig. 7(d). We observe an almost Ohmic behavior. The same behavior is also observed for sample *C*. Most important for the discussion of our results are the *I-V* responses for the QD excitation, as shown in Figs. 7(e) and 7(f) for samples *C* and *A*, respectively. All responses in the positive and negative branches are almost perfectly linear, with a consequently higher EQE for sample *C*. This result indicates that our conclusion of lower EQE for the high-density QD sample is independent of the contact type.

APPENDIX D: CALCULATION MODEL

For simulating the effect of a charging of the QD traps on the IR PC, we numerically solve the one-dimensional (1D) continuity equation

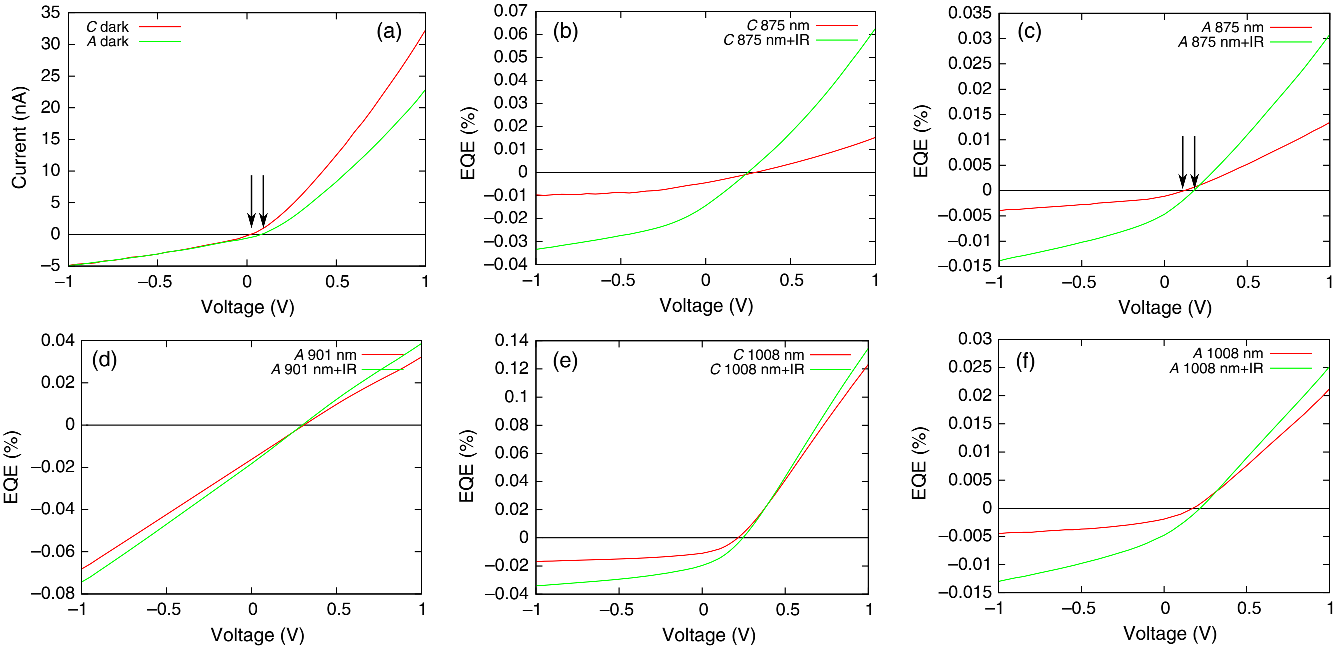

FIG. 7. (a) Dark *I-V* curves. (b)–(f) *I-V* curves for different excitation wavelengths. The value of the current is converted to EQE by subtracting the corresponding dark current and normalized by the input photon flux of the primary beam. EQE is positive when holes flow to the surface and electrons to the back side.

$$\frac{dn(x,t)}{dt} = \mu_n \frac{dE(x,t)n(x,t)}{dx} + D_n \frac{d^2 n(x,t)}{dx^2} + G(x,t) - R(x,t). \tag{D1}$$

A similar equation is used for the hole density $p(x)$. The mobility of the electrons and the holes is assumed to be $\mu_n = 2000$ and $\mu_p = 200\ \mathrm{cm^2/V\,s}$, respectively. The electric field is given by $E(x)$, and the diffusion constant D_n is taken as $\mu_n k_B T$ (k_B is the Boltzmann constant, $T = 300$ K). Generation G is assumed to be constant throughout the sample and consists of thermal generation $G_{\mathrm{th}} = n_i^2 B$ (equal to the local-equilibrium thermal PL) and light-induced excitation G_{ex}. The bimolecular constant B is $1.1 \times 10^{-10}\ \mathrm{cm^3/s}$. The GaAs intrinsic carrier density is $n_i = 2 \times 10^6\ \mathrm{cm^{-3}}$. For the light-induced generation, we apply the same total photon flux as in the experiment (3.1×10^{12}/s) and assume complete absorption within the calculation volume. The recombination R consists of Shockley-Read-Hall (SRH) recombination R_{SRH} ($\tau_{\mathrm{SRH}} = 40$ ns) of free carriers and the PL throughout the total volume. The number of holes trapped in the QD-induced trap sites is assumed to be one sixth of the QD density measured by AFM. The photoluminescence is assumed to be purely bimolecular, i.e., $PL = pnB$.

For the electrical circuit, we assume an Ohmic contact. The electron flow through the contact is proportional to the difference to the equilibrium carrier density. The voltage source is simulated by maintaining a constant charge offset between both contacts, corresponding to a voltage of 0.1 V. The sample thickness is set at 30 μm, and we use a spatial resolution of 50 nm. The temporal resolution is 100 fs. The effect of electron drift-velocity saturation is implemented as a step function, occurring at 500 V/cm, which is roughly 10 times smaller than in reality. This value is chosen in accordance with the roughly 10-times-longer distance of the QDs from the surface, in order to ensure small derivation errors for the present spatial resolution.

The density profiles for electrons and holes for the same excitation with and without filled QD traps are shown in Figs. 8(a) and 8(b), respectively. It is obvious that the hole trap density ($10^{10}/\mathrm{cm^2}$) drastically alters the carrier-density profiles. Without traps, the holes tend to the left and the electrons to the right, as expected due to the electric field [Fig. 8(b)]. However, the electrons will be centered around the QD layer if they are positively charged with holes. This redistribution induces a strong diffusion current towards the surface, which can overcome the drift velocity and induces a negative-current component.

The correctness of the calculated density profiles is confirmed by comparing the equilibrium (no contact) and steady-state (with Ohmic contact) conditions in the dark and under bias with the results from an industry-standard 1D solar-cell device simulator (PC1D), as shown in Figs. 9(a) and 9(b) [50]. These results are for purely radiative recombination. The open-circuit condition in Fig. 9(a) agrees very well with the result from PC1D.

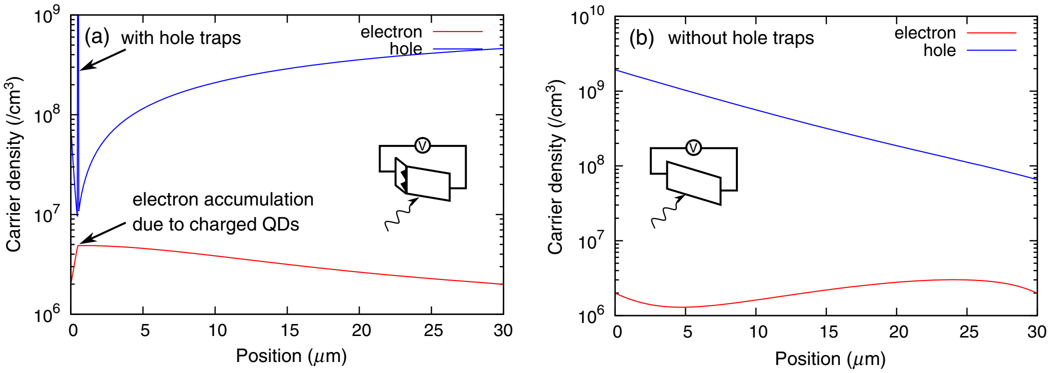

FIG. 8. (a) Carrier densities in the case of trapped holes in the QD layer (at 500 nm) under light excitation for a bias of 0.1 V and a closed circuit. (b) Carrier densities in a sample without traps under light excitation for a bias of 0.1 V and a closed circuit.

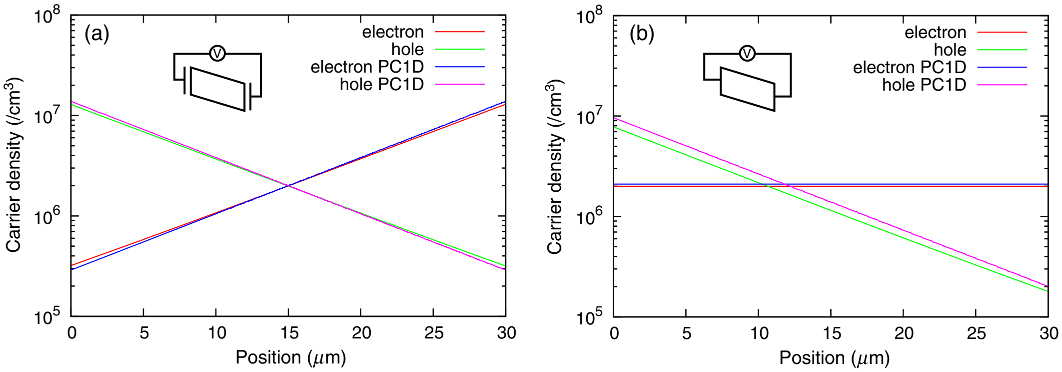

FIG. 9. (a) Carrier densities for a bias of 0.1 V and an open circuit. (b) Carrier densities for a bias of 0.1 V and a closed circuit.

The current for 0.1-V bias and the connected circuit [Fig. 9(b)] is almost the same as that predicted from the theory ($j = q\mu nE = 22$ nA) in both cases. The small differences in the density between the steady-state solution of the continuum equation and PC1D are partly explained by the finite calculation time and the nonideal contact properties in the PC1D model.

[1] W. Shockley and H. J. Queisser, Detailed balance limit of efficiency of *p-n* junction solar cells, J. Appl. Phys. **32**, 510 (1961).

[2] M. Wolf, Limitations and possibilities for improvement of photovoltaic solar energy converters: Part I: Considerations for earth's surface operation, Proc. IRE **48**, 1246 (1960).

[3] F. Dimroth and S. Kurtz, High-efficiency multijunction solar cells, MRS Bull. **32**, 230 (2007).

[4] B. M. Kayes, H. A. Atwater, and N. S. Lewis, Comparison of the device physics principles of planar and radial *p-n* junction nanorod solar cells, J. Appl. Phys. **97**, 114302 (2005).

[5] E. C. Garnett and P. Yang, Silicon nanowire radial *p-n* junction solar cells, J. Am. Chem. Soc. **130**, 9224 (2008).

[6] S. Qian, S. Misra, J. Lu, Z. Yu, L. Yu, J. Xu, J. Wang, L. Xu, Y. Shi, K. Chen, and P. R. i Cabarrocas, Full potential of radial junction Si thin film solar cells with advanced junction materials and design, Appl. Phys. Lett. **107**, 043902 (2015).

[7] I. M. Dharmadasa, Third generation multi-layer tandem solar cells for achieving high conversion efficiencies, Sol. Energy Mater. Sol. Cells **85**, 293 (2005).

[8] T. Dennis, in *Proceedings of the 39th Photovoltaics Specialists Conference (PVSC), Tampa, 2013* (IEEE, New York, 2013), p. 81.

[9] D. M. Tex, T. Ihara, H. Akiyama, M. Imaizumi, and Y. Kanemitsu, Time-resolved photoluminescence measurements for determining voltage-dependent charge-separation efficiencies of subcells in triple-junction solar cells, Appl. Phys. Lett. **106**, 013905 (2015).

[10] D. M. Tex, M. Imaizumi, and Y. Kanemitsu, Charge separation in subcells of triple-junction solar cells revealed by time-resolved photoluminescence spectroscopy, Opt. Express **23**, A1687 (2015).

[11] A. W. Walker, S. Heckelmann, C. Karcher, O. Höhn, C. Went, M. Niemeyer, A. W. Bett, and D. Lackner, Nonradiative lifetime extraction using power-dependent relative photoluminescence of III-V semiconductor double-heterostructures, J. Appl. Phys. **119**, 155702 (2016).

[12] A. Luque and A. Marti, Increasing the Efficiency of Ideal Solar Cells by Photon Induced Transitions at Intermediate Levels, Phys. Rev. Lett. **78**, 5014 (1997).

[13] A. Marti, E. Antolin, C. R. Stanley, C. D. Farmer, N. Lopez, P. Diaz, E. Canovas, P. G. Linares, and A. Luque, Production of Photocurrent due to Intermediate-to-Conduction-Band Transitions: A Demonstration of a Key Operating Principle of the Intermediate-Band Solar Cell, Phys. Rev. Lett. **97**, 247701 (2006).

[14] A. Luque, A. Marti, and C. Stanley, Understanding intermediate-band solar cells, Nat. Photonics **6**, 146 (2012).

[15] D. Leonard, M. Krishnamurthy, C. M. Reaves, S. P. Denbaars, and P. Petroff, Direct formation of quantum-sized dots from uniform coherent islands of InGaAs on GaAs surfaces, Appl. Phys. Lett. **63**, 3203 (1993).

[16] A. Datas, E. Lopez, I. Ramiro, E. Antolin, A. Marti, A. Luque, R. Tamaki, Y. Shoji, T. Sogabe, and Y. Okada, Intermediate Band Solar Cell with Extreme Broadband Spectrum Quantum Efficiency, Phys. Rev. Lett. **114**, 157701 (2015).

[17] A. Luque, A. Marti, N. Lopez, E. Antolin, E. Canovas, C. Stanley, C. Farmer, L. J. Caballero, L. Cuadra, and J. L. Balenzategui, Experimental analysis of the quasi-Fermi level split in quantum dot intermediate-band solar cells, Appl. Phys. Lett. **87**, 083505 (2005).

[18] S. M. Hubbard, C. D. Cress, C. G. Bailey, R. P. Raffaelle, S. G. Bailey, and D. M. Wilt, Effect of strain compensation on quantum dot enhanced GaAs solar cells, Appl. Phys. Lett. **92**, 123512 (2008).

[19] R. Oshima, A. Takata, and Y. Okada, Strain-compensated InAs/GaNAs quantum dots for use in high-efficiency solar cells, Appl. Phys. Lett. **93**, 083111 (2008).

[20] D. Guimard, R. Morihara, D. Bordel, K. Tanabe, Y. Wakayama, M. Nishioka, and Y. Arakawa, Fabrication of InAs/GaAs quantum dot solar cells with enhanced photocurrent and without degradation of open circuit voltage, Appl. Phys. Lett. **96**, 203507 (2010).

[21] K. A. Sablon, J. W. Little, V. Mitin, A. Sergeev, N. Vagidov, and K. Reinhardtz, Strong enhancement of solar cell efficiency due to quantum dots with built-in charge, Nano Lett. **11**, 2311 (2011).

[22] T. Kita, T. Maeda, and Y. Harada, Carrier dynamics of the intermediate state in InAs/GaAs quantum dots coupled in a photonic cavity under two-photon excitation, Phys. Rev. B **86**, 035301 (2012).

[23] X. Yang, K. Wang, Y. Gu, H. Ni, X. Wang, T. Yang, and Z. Wang, Improved efficiency of InAs/GaAs quantum dots solar cells by Si-doping, Sol. Energy Mater. Sol. Cells **113**, 144 (2013).

[24] G. Jolley, L. Fu, H. F. Lu, H. H. Tan, and C. Jagadish, The role of intersubband optical transitions on the electrical properties of InGaAs/GaAs quantum dot solar cells, Prog. Photovoltaics **21**, 736 (2013).

[25] C. B. Honsberg, S. P. Bremner, and R. Corkish, Design trade-offs and rules for multiple energy level solar cells, Physica (Amsterdam) **14E**, 136 (2002).

[26] E. Antolin, A. Marti, C. D. Farmer, P. G. Linares, E. Hernandez, A. M. Sanchez, T. Ben, S. I. Molina, C. R. Stanley, and A. Luque, Reducing carrier escape in the InAs/GaAs quantum dot intermediate-band solar cell, J. Appl. Phys. **108**, 064513 (2010).

[27] D. M. Tex, I. Kamiya, and Y. Kanemitsu, Control of hot-carrier relaxation for realizing ideal quantum-dot intermediate-band solar cells, Sci. Rep. **4**, 4125 (2014).

[28] D. G. Sellers, S. Polly, S. M. Hubbard, and M. F. Doty, Analyzing carrier escape mechanisms in InAs/GaAs quantum dot p-i-n junction photovoltaic cells, Appl. Phys. Lett. **104**, 223903 (2014).

[29] M. Elborg, T. Noda, T. Mano, M. Jo, Y. Sakuma, K. Sakoda, and L. Han, Voltage dependence of two-step photocurrent generation in quantum dot intermediate band solar cells, Sol. Energy Mater. Sol. Cells **134**, 108 (2015).

[30] S. Tomic, T. S. Jones, and N. M. Harrison, Absorption characteristics of a quantum dot array induced intermediate-band: Implications for solar cell design, Appl. Phys. Lett. **93**, 263105 (2008).

[31] R. Strandberg and T. W. Reenaas, Photofilling of intermediate bands, J. Appl. Phys. **105**, 124512 (2009).

[32] V. Popescu, G. Bester, M. C. Hanna, A. G. Norman, and A. Zunger, Theoretical and experimental examination of the intermediate-band concept for strain-balanced $(\mathrm{In,Ga})\mathrm{As}/\mathrm{Ga}(\mathrm{As},P)$ quantum dot solar cells, Phys. Rev. B **78**, 205321 (2008).

[33] K. Sakamoto, Y. Kondo, K. Uchida, and K. Yamaguchi, Quantum-dot density dependence of power conversion efficiency of intermediate-band solar cells, J. Appl. Phys. **112**, 124515 (2012).

[34] R. Tamaki, Y. Shoji, Y. Okada, and K. Miyano, Spectrally resolved intraband transitions on two-step photon absorption in InGaAs/GaAs quantum dot solar cell, Appl. Phys. Lett. **105**, 073118 (2014).

[35] R. Heitz, T. R. Ramachandran, A. Kalburge, Q. Xie, I. Mukhametzhanov, P. Chen, and A. Madhukar, Observation of Reentrant 2D to 3D Morphology Transition in Highly Strained Epitaxy: InAs on GaAs, Phys. Rev. Lett. **78**, 4071 (1997).

[36] D. M. Tex and I. Kamiya, Upconversion of infrared photons to visible luminescence using InAs-based quantum structures, Phys. Rev. B **83**, 081309(R) (2011).

[37] D. M. Tex, I. Kamiya, and Y. Kanemitsu, Efficient upconverted photocurrent through an Auger process in disklike InAs quantum structures for intermediate-band solar cells, Phys. Rev. B **87**, 245305 (2013).

[38] I. Kamiya, D. M. Tex, K. Shimomura, F. Yamada, K. Takabayashi, and Y. Kanemitsu, in *Proceedings of the 39th Photovoltaics Specialists Conference (PVSC), Tampa, 2013* (IEEE, New York, 2013), p. 3040.

[39] D. M. Tex, T. Ihara, I. Kamiya, and Y. Kanemitsu, Microscopic photoluminescence and photocurrent imaging spectroscopy of InAs nanostructures: Identification of photocarrier generation sites for intermediate-band solar cells, Phys. Rev. B **89**, 125301 (2014).

[40] D. M. Tex, T. Ihara, I. Kamiya, and Y. Kanemitsu, Temperature and light-intensity dependence of upconverted photocurrent generation in shallow InAs quantum structures, Jpn. J. Appl. Phys. **53**, 05FV01 (2014).

[41] D. M. Tex, I. Kamiya, and Y. Kanemitsu, in *Proceedings of the 40th IEEE Photovoltaic Specialists Conference (PVSC), Denver, 2014* (IEEE, New York, 2014), p. 3618.

[42] Y. Yamada, D. M. Tex, I. Kamiya, and Y. Kanemitsu, Femtosecond upconverted photocurrent spectroscopy of InAs quantum nanostructures, Appl. Phys. Lett. **107**, 013905 (2015).

[43] E. J. Johnson, J. Kafalas, R. W. Davies, and W. A. Dyes, Deep center EL2 and anti-Stokes luminescence in semi-insulating GaAs, Appl. Phys. Lett. **40**, 993 (1982).

[44] K. Yoshida, Y. Okada, and N. Sano, Self-consistent simulation of intermediate band solar cells: Effect of occupation rates on device characteristics, Appl. Phys. Lett. **97**, 133503 (2010).

[45] Y. Okada, T. Morioka, K. Yoshida, R. Oshima, Y. Shoji, T. Inoue, and T. Kita, Increase in photocurrent by optical transitions via intermediate quantum states in direct-doped InAs/GaNAs strain-compensated quantum dot solar cell, J. Appl. Phys. **109**, 024301 (2011).

[46] A. Marti, L. Cuadra, and A. Luque, in *Proceedings of the 28th IEEE Photovoltaic Specialists Conference (PVSC), Anchorage, 2000* (IEEE, New York, 2000), p. 940.

[47] Y. Okada, K. Yoshida, Y. Shoji, A. Ogura, P. G. Linares, A. Marti, and A. Luque, The effect of concentration on the performance of quantum dot intermediate-band solar cells, AIP Conf. Proc. **1477**, 10 (2012).

[48] D. Ricci and P. C. Braga, Recognizing and avoiding artifacts in AFM imaging, Methods Mol. Biol. (N.Y.) **242**, 25 (2004).

[49] National Institute of Standards and Technology, Nanotechnology Characterization Laboratory, Size measurement of nanoparticles using atomic force microscopy, http://ncl.cancer.gov (2009).

[50] D. A. Clugston and P. A. Basore, in *Proceedings of the 26th IEEE Photovoltaic Specialists Conference (PVSC), Anaheim, 1997* (IEEE, New York, 1997), p. 207.